Journal of Computational Chemistry

WILEY

Journal of COMPUTATIONAL CHEMISTRY

RESEARCH ARTICLE

Heterogeneous Autoxidation of VOCs Promotes Light-Scattering of Atmospheric Mineral Particle: A DFT Study

Weina Zhang[1,2] | Zhichao Fan[1] | Yao Zhou[1] | Kaixin Zhang[1]

[1]Guangdong Key Laboratory of Environmental Catalysis and Health Risk Control, Guangdong-Hong Kong-Macao Joint Laboratory for Contaminants Exposure and Health, Institute of Environmental Health and Pollution Control, Guangdong University of Technology, Guangzhou, China | [2]Guangzhou Key Laboratory of Environmental Catalysis and Pollution Control, Key Laboratory of City Cluster Environmental Safety and Green Development of Ministry of Education, Basic Research Center of Excellence for Ecological Security and Green Development, School of Environmental Science and Engineering, Guangdong University of Technology, Guangzhou, China

Correspondence: Weina Zhang (zhangwn@gdut.edu.cn)

Received: 6 June 2025 | **Revised:** 12 July 2025 | **Accepted:** 17 July 2025

Funding: This work was supported by NSFC (42277081 and 42077189), the Basic and Applied Basic Research Fund Project of Guangdong Province (2024A1515012691), the National Key Research and Development Program of China (2022YFC3105600), and the GuangZhou Basic and Applied Basic Research Foundation (2025A04J5188).

Keywords: DFT calculations | heterogeneous autoxidation | light-scattering | VOCs

ABSTRACT

Recently, the heterogeneous autoxidation of volatile organic compounds (VOCs) has been shown to alter the light-scattering property of atmospheric mineral particles. Here, we investigate how VOCs with different central atoms dictate autoxidation pathways and subsequent highly oxygenated molecules (HOMs) properties, ultimately influencing the complex refractive index of VOC-mineral particles via density functional theory (DFT) and quantitative structure–property relationship (QSPR) analysis. Using dimethylsulfide (DMS)/dimethylether (DME) as ether-type proxies and triethylamine (TEA)/trimethylphosphine (TMP) as alkane-type proxies, we reveal two distinct autoxidation paths: alkane-type VOCs undergo more O_2-addition steps due to their structural capacity for H-shift reactions, generating HOMs with higher oxidation states (OS), molar mass, and polarizability. These properties drive stepwise increases in the refractive index (n) for alkane-VOC-mineral particles, leading to stronger light-scattering ability compared to ether-type counterparts. Our results establish a direct link between VOCs' autoxidation mechanisms and optical properties, providing new insights into climate-relevant aerosol interactions.

1 | Introduction

Mineral particles exert a significant cooling radiative forcing effect (RFE) on the global climate, with emissions of 4300 $Tg\,y^{-1}$ into the atmosphere [1]. Previously, considerable attention has been paid to the promotional effect of mineral particles on the heterogeneous reactions of volatile organic compounds (VOCs) [2–4]. However, this attention has recently been drawn to the fact that the heterogeneous reactions of VOCs might, in turn, alter the cooling RFE of mineral particles. For instance, the net cooling RFE of black carbon–mineral particle is enhanced by 7.4% and 6.5% compared to the individual black carbon and

Abbreviations: CDD, Charge density difference; DFT, Density functional theory; DME, Dimethylether; DMS, Dimethylsulfide; GGA, Generalized gradient approximation; HOMs, Highly oxygenated molecules; IM, Intermediate; Kao, Kaolinite; OS, Oxidation states; PBE, Perdew–Burke–Ernzerhof; PES, Potential energy surface; Pro, Product; QSPR, Quantitative structure–property relationship; RC, Reactant; RFE, Radiative forcing effect; SOAs, Secondary organic aerosols; TEA, Triethylamine; TMP, Trimethylphosphine; TS, Transition state; VASP, Vienna Ab initio Simulation Package; VOCs, Volatile organic compounds.

mineral particle, respectively [5, 6]. Very recently, our theoretical work has revealed that amines proceed with faster H-shift autoxidation reactions on clay particle surface, which, in turn, enhances the cooling RFE of clay particles by 27.1%–47.1% under visible light [7]. Moreover, the cooling RFE enhancement resulting from autoxidation is at least 11.3% higher than that caused by other oxidations [7]. Therefore, computational focus should prioritize elucidating how autoxidation mechanisms of diverse VOCs modulate the cooling RFE of mineral particles, particularly the differential impacts governed by their molecular structures.

Autoxidation of VOCs constitutes the dominant formation pathway for secondary organic aerosols (SOAs) [8–11], which exert significant influences on climate change through their cooling RFE via light scattering [12–14]. Produced highly oxygenated molecules (HOMs) not only contribute to aerosol mass but also elevate the oxidation state (OS) of SOAs [8, 10, 15, 16]. Previous experimental studies have observed that increased OS during aerosol aging—such as in guaiacol-, α-pinene-, and p-xylene-derived SOAs—leads to complex changes in light-scattering properties [17–19]. However, the mechanistic link between VOC molecular structure, autoxidation pathways, and resulting optical property modifications remains unclear, particularly how structural features of VOCs dictate the formation of HOMs with distinct OS and chemical compositions.

Autoxidation of VOCs is initiated by H-abstraction, forming radicals (•R) [20] that undergo either O_2-addition-driven H-shift (alkane-type VOCs) or limited oxidation (ether-type VOCs). Molecular structure, defined by central heteroatoms (N, O, S, P) and substituent groups, is critical: alkane-type VOCs (e.g., TEA, TMP) possess more methyl (—CH_3) groups, providing additional sites for H-shift reactions that enable sequential O_2-addition [21–23]. In contrast, ether-type VOCs (e.g., DMS, DME) have fewer H-shift sites due to their oxygen/sulfur-centered structures, restricting O_2-addition steps [24–26]. These structural differences lead to HOMs with distinct oxidizing states (OS) and chemical compositions, directly impacting the optical properties of mineral particles.

Previous studies have shown that HOMs enhance light scattering by increasing particle refractive index, a key determinant of light scattering. However, the role of VOC molecular structure in regulating autoxidation pathways and subsequent HOM properties remains unclear. Here, we address this gap by systematically comparing ether-type and alkane-type VOCs, revealing how their structural features dictate autoxidation mechanisms, HOM characteristics, and ultimately light-scattering parameters of mineral particles. DMS and DME are chosen as ether-type proxies, and TMP and TEA are chosen as alkane-type proxies, respectively. Kaolinite (Kao) is chosen as the proxy of mineral particle because of its large emission to atmosphere (192.3 Tg y^{-1}) [27].

2 | Computational Methods

Static DFT calculations are carried out using the Vienna Ab initio Simulation Package (VASP) [28]. Van der Waals interactions are described using the exchange–correlation functional of Perdew–Burke–Ernzerhof (PBE) generalized gradient approximation (GGA) [29]. The electron–core interactions are described with the projector augmented wave method. Furthermore, dispersion corrections of the D3 type were incorporated into the calculations [30, 31]. Simulated supercells are sampled with gamma-centered 3×3×1 Monkhorst-Pack grids for the integration of the Brillouin zone. To ensure the efficiency and reliability of calculation, the kinetic cutoff energy is set at 400 eV, and the convergence criterion of structural optimization is −0.01 eV $Å^{-1}$.

VOC-Kao particles models are composed of Kao surface and DMS/TEA/DME/TMP molecule. Kao surface is cleaved from Kao unit cell along (001) direction and expanded to the size of 2×1. A vacuum zone of 15 Å is added onto Kao surface to eliminate the interaction of each layer. VOC molecule is separately added above Kao surface. The adsorption energy of VOC by Kao surface (ΔE_{ads}) equals $E_{VOC\text{-}Kao}$—E_{VOC}—E_{Kao}. The related structures and ΔE_{ads} results are summarized in Figure S1A–D. Negative ΔE_{ads} values indicate VOC adsorption on Kao surface is feasible at ambient condition.

The geometry, frequency, and single point energy of each reactant (RC), intermediate (IM), product (Pro) and transition state (TS) are determined via density function theory calculations, which are carried out with the Vienna Ab Initio Simulation Package [28]. Thereinto, TS is searched via the climbing image nudged elastic band [32] and identified with only one imaginary mode. Along the potential energy surface (PES), the energy barrier ($\Delta E^{\neq}$) is E_{TS}—E_{RC}, and the reaction energy (ΔE_r) is $E_{Pro/IM}$—E_{RC}. Accordingly, rate constants (k) are described as follows [33]:

$$k = \sigma\kappa\frac{k_B T}{h}e^{-\frac{\Delta E^{\neq}}{RT}} \quad (1)$$

$$k = \sigma\kappa\frac{k_B T}{h}\left(\frac{k_B T}{P_0}\right)e^{-\frac{\Delta E_r^{\neq}}{RT}} \quad (2)$$

where Equation (1) is for the first-order reaction constants and Equation (2) is for the second-order rate constants, respectively. σ is reaction path degeneracy, κ is the Eckart tunneling coefficient, k_B is the Boltzmann constant, T is the temperature, h is Planck's constant, and P_0 is standard atmospheric pressure. All the $\Delta E^{\neq}$ and k for each reaction step are displayed in Table S1.

In this study, the oxidation state (OS) was employed to characterize the oxidative status of DMS/DME/TMP/TEA-Kao mixed particles. For typical hydrocarbons (e.g., alkanes or aromatic hydrocarbons), the oxidation state is defined as $OS = n_{C-O} - n_{C-H}$, where n_{C-O} and n_{C-H} represent the number of formed C—O bonds and total C—H bonds, respectively [34]. This formulation remains applicable to saturated alkanes with central atoms of N, O, P, and S. Notably, the OS values remain constant during the oxidation phase from RO_2• to ROOOH in DMS/TEA-Kao mixed particles. This phenomenon arises because the oxidation process from RO_2• to ROOOH formation does not involve changes in the number of C—O and C—H bonds. Distinct oxidation stages are therefore differentiated using the suffixes a, b or c, d to denote specific transition phases.

To describe light scattering of VOC-Kao particles, refractive index (n) and extinction coefficient (p) of each VOC-Kao

particle are calculated from complex dielectric function [35] and Kramers-Kronig relation [36, 37].

3 | Results and Discussion

3.1 | VOC Adsorption on Kao Competing With Gas Oxidation

The adsorption configurations were optimized using DFT. As depicted in Figure 1, each VOC is combined with the Kao surface with 1–2 hydrogen bonds. Each hydrogen bond is formed between centered atoms of VOC and the hydrogen atom of Kao's surface. The differential charge density difference (CDD) results display negative charge distributions on these centered atoms of VOCs and positive charge distributions on the hydrogen atoms of Kao's surface. The stability of these hydrogen bonds is contributed to by the coulomb interaction. Resultingly, negative adsorption energy values (ΔE_{ads}) of VOCs are determined. Specifically, ΔE_{ads} is −12.56 kcal/mol for DMS, −14.20 kcal/mol for DME, −13.18 kcal/mol for TMP, and −17.51 kcal/mol for TEA, respectively. Therefore, each VOCs is chemically adsorbed to Kao's surface, which supports the following heterogeneous autoxidation reactions.

The competitive relationship between the heterogeneous autoxidation of each and their gas-phase oxidation by OH is determined by r_1/r_2, where r_1 and r_2 represent the adsorption rate and the initial step of the gas-phase oxidation, respectively. r_1 is obtained by k_1[Kao][VOC], and r_2 is obtained by k_2[•OH][VOC], where k_1 and k_2 represent the rate constants for the adsorption of VOC and the initial step of their gas-phase oxidation. Therefore, r_1/r_2 equals $(k_1[\text{Kao}])/(k_2[\bullet\text{OH}])$. Based on present adsorption energy values of each VOC (Figure 1) and Equation (2), k_1 is $4.15\times10^{2}\,cm^3\,molec^{-1}\,s^{-1}$ for DMS, $6.63\times10^{3}\,cm^3\,molec^{-1}\,s^{-1}$ for DME, $1.18\times10^{3}\,cm^3\,molec^{-1}\,s^{-1}$ for TMP, and $1.77\times10^{6}\,cm^3\,molec^{-1}\,s^{-1}$ for TEA, respectively. k_2 for DMS and DME is 5.9×10^{-13} and $1.1\times10^{-12}\,cm^3\,molec^{-1}\,s^{-1}$, respectively [38], and for TMP and TEA is 1.4×10^{-11} and $6.84\times10^{-12}\,cm^3\,molec^{-1}\,s^{-1}$, respectively [39]. Besides, [Kao] is approximately $6.1\times10^{21}\,molec\,cm^{-3}$, and [•OH] in the atmosphere is about $2.4\times10^{6}\,molec\,cm^{-3}$ [40, 41]. Accordingly, r_1/r_2 is calculated to be 1.79×10^{30} for DMS, 1.53×10^{31} for DME, 2.14×10^{29} for TMP, and 6.57×10^{32} for TEA, respectively. These results indicate that the adsorption of VOCs occurs prior to their initial step of gas-phase oxidation, proving that their heterogeneous autoxidation will compete with their gas-phase oxidation reactions.

3.2 | Two Heterogeneous Autoxidation Paths

Based on the corresponding PES (Figure 2), DMSDME/TMP/TEA initially undergo heterogeneous H-abstraction reactions with •OH on the Kao surface. Corresponding structures can be found in Figure S1A–D. Consequently, •R for each VOC is formed separately through exothermic reactions under ambient conditions. For DMS, DME, and TMP, their •R formation processes are completely the same, namely that the H-abstraction merely occurs on their —CH_3 groups (Figure 2a). For DME, its $\Delta E^{\neq}$ is calculated as 8.3 kcal/mol, and the resulting k is $9.41\times10^{-13}\,s^{-1}\,molec^{-1}\,cm^3$. By contrast, for DMS and TMP, their $\Delta E^{\neq}$ values are negative, which are −3.8 and −1.6 kcal/mol, respectively. The resulting k values are 9.59×10^{-4} and $2.18\times10^{-5}\,s^{-1}\,molec^{-1}\,cm^3$ respectively, which represent an increase of 9 and 8 orders of magnitude compared to that of DME. Considering the k values of the above three VOCs, their •R is easily formed on the Kao surface. As for TEA, Figure 2b shows that H-abstraction could occur on its α-site or β-site of its —CH_2CH_3 substitution. As the $\Delta E^{\neq}$ for α-site is 14.8 kcal/mol lower than that for β-site, the former is the dominant H-abstraction path of TEA. The related k of TEA's H-abstraction is $5.71\times10^{1}\,s^{-1}\,molec^{-1}\,cm^3$, implying it proceeds easily under ambient conditions. Therefore, like the other three VOCs, •R of TEA is also formed on the terminal carbon. In summary, the conversion from each VOC to the related •R is the same under ambient conditions, which is not related to their alkane or ether structure at this stage.

Each •R continues to react with O_2 through no-barrier and exothermic steps, spontaneously converting into RO_2• under ambient conditions. RO_2• is CH_3—S—CH_2OO• for DMS, CH_3—O—CH_2OO• for DME, $(CH_3)_2$—P—CH_2OO• for TMP,

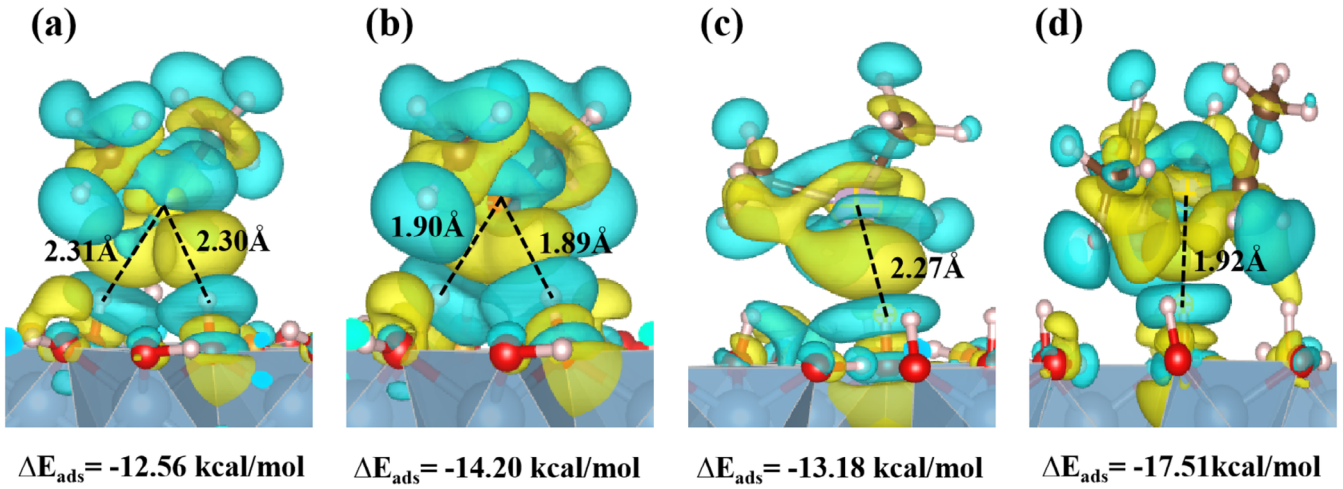

FIGURE 1 | The differential charge densities of four VOCs on the Kao surface and their corresponding adsorption energies. (a) DMS, (b) DME, (c) TMP, and (d) TEA. Blue bubbles represent negative charge distributions, and yellow bubbles represent positive charge distributions.

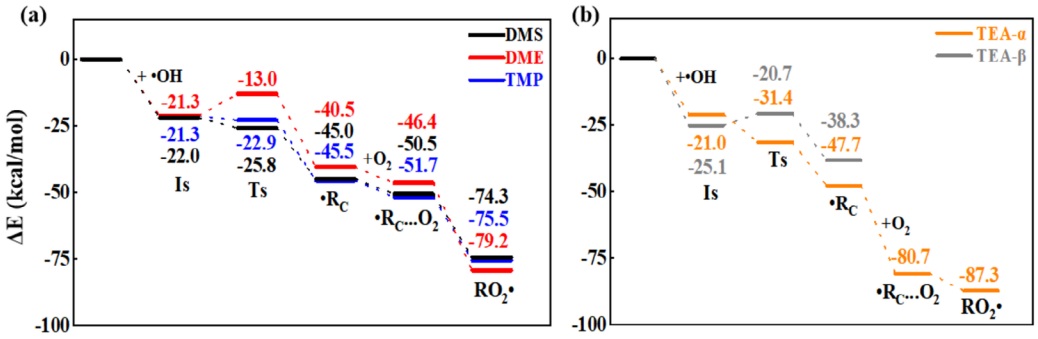

FIGURE 2 | Initial oxidation of the four VOCs and • OH/O_2. (a) PESs for DMS, DME, and TMP, (b) PES for TEA.

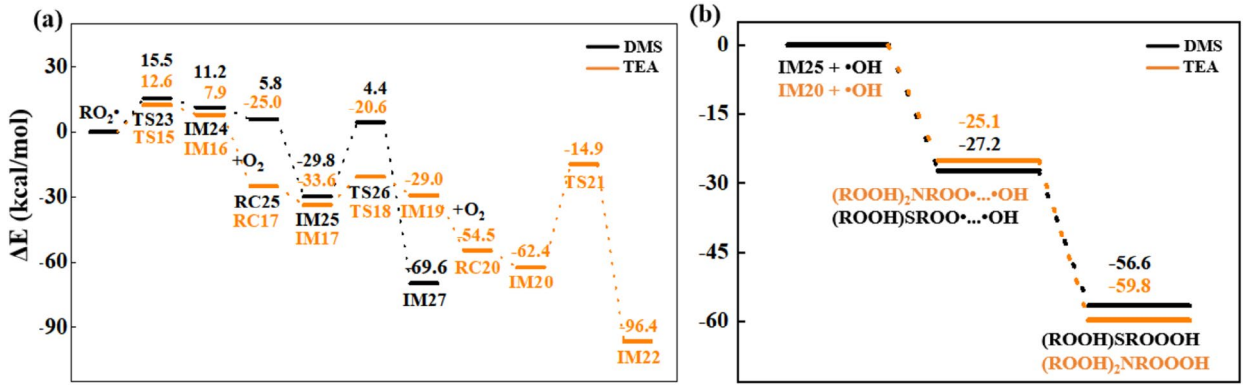

FIGURE 3 | Uncompleted autoxidation reactions of RO_2• along path1. (a) PES of the key intermediate formations from DMS and TEA, (b) PES of HOMs yields for DMS and TEA.

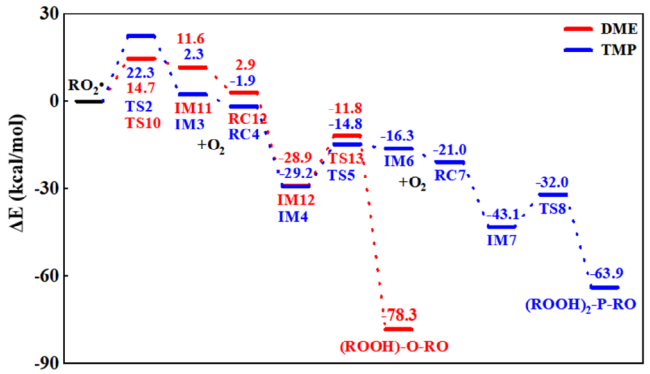

FIGURE 4 | Completed autoxidation reactions of RO_2• along path2. The PESs describe the key intermediate and HOMs formations for DMS and TMP.

and $(CH_2CH_3)_2$—N—CH_2OOCH_3 for TEA, respectively. Corresponding structures can be found in Figure S1A–D. RO_2• is produced for the oxidation of alkane-type and ether-type VOCs and also generates unique HOMs through two distinct autoxidation pathways. As depicted in Figure 3, DMS and TEA generate HOMs of $(ROOH)_n$—X—ROOOH (X = S or N) via incomplete autoxidation (path 1): their RO_2• radicals initially undergo a sequence of hydrogen shifts and oxygen addition steps, culminating in the addition of •OH [42]. For DMS, it only proceeds with one step of O_2-addition (black line in Figure 3a), producing (ROOH)—S—ROOOH (black line in Figure 3b). Similarly, TEA proceeds with two steps of O_2-addition (orange line in Figure 3a), producing $(ROOH)_2$—N—ROOOH (orange line in Figure 3b). Therefore, the OS of HOMs for TEA is two larger than that for DMS. Different from DMS and TEA, DME and TMP carry out completed autoxidation and produce HOMs of $(ROOH)_n$—X—RO (X = O or P) (path2). Corresponding structures can be found in Figure S1A–D. Yet, like TEA versus DMS, $(ROOH)_2$—P—RO generated from TMP exhibits higher OS than (ROOH)—O—RO produced from DME (Figure 4). This is because the former carries out one more O_2-addition step. Therefore, the OS levels of HOM products are directly determined by molecular structures of initial VOCs. Specifically, alkane-type VOC produces HOMs with higher OS levels than ether-type VOCs. Based on the above analysis, this is chemically determined by the number of oxygen addition steps. The alkane structure has one more methyl group than the ether structure, providing more H-shift sites.

Moreover, the thermodynamic and kinetic feasibility of the rate-limiting hydrogen-shift (H-shift) step governs the initiation barrier for subsequent O_2-addition reactions. Along path1, the lowest k for DMS and TEA are separately 3.64×10^{-12} and $2.26\times10^{-22}\,s^{-1}$ (R5 of DMS and R7 of TEA, Table S1). This indicates their last H-shift steps would be difficult under ambient conditions and be replaced by the OH-addition step. Therefore, DMS and TEA carry out an incomplete path, resulting in higher OS of HOMs products. Comparatively, along path2, the lowest k for DME is $1.04\times10^{1}\,s^{-1}$ (R6 of DME, Table S1) and for TMP is $2.72\times10^{-3}\,s^{-1}$ (R3 of TMP, Table S1), respectively, implying their rate-limiting H-shift steps quickly proceed under the same conditions. Accordingly, DME and TMP proceed with a completed autoxidation path.

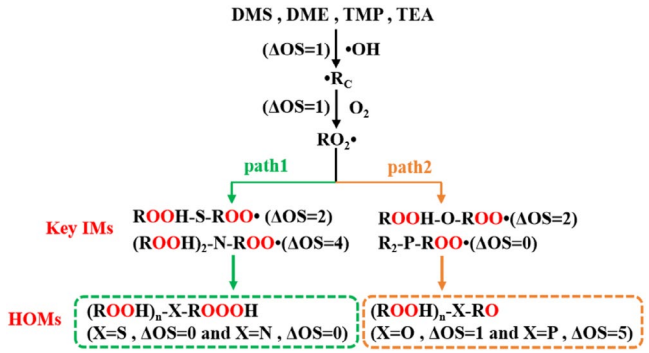

FIGURE 5 | Heterogeneous oxidation mechanism of DMS/DME/TMP/TEA on Kao surface. X = S, O, P, or N, and n = 1 or 2.

Based on present results, the heterogeneous autoxidation mechanisms of DMS, TEA, DME, and TMP on Kao surface are summarized in Figure 5. The four VOCs are converted into •R, RO_2•, key intermediates of H-shift steps in order, leading to two types of HOMs yields of variable OS on Kao surface. Firstly, negative adsorption energy values of reactants, key intermediates, and products imply that they are chemically adsorbed by Kao surface. Moreover, their atomic structures illustrate that they are bonded through stable hydrogen bonds formed between central atoms of the four VOCs and exposed hydrogen atoms of Kao surface (Figure S1). Therefore, the heterogeneous autoxidation of the four VOCs is confirmed to proceed on Kao surfaces, potentially affecting the light scattering property of VOC-Kao particles.

Next, from initial VOCs to their RO_2•, the related ΔOS level is the same. Note, RO_2• of DMS and TEA continues to proceed with an uncompleted autoxidation path (path1), and the other two RO_2• carry out a completed path (path2), generating two types of HOMs yields with different ΔOS. It is interesting that DMS (or TEA) and DME (or TMP) are both ether-type (or alkane-type) VOCs but proceed with different heterogeneous autoxidation paths. To reveal why this occurs, the reactivity of key intermediates of the rate-limiting H-shift step is analyzed by combining Bader charge calculation and H-shift distances (Figure S2). Along path1, two key intermediates are ROOH—S—ROO• for DMS and $(ROOH)_2$—N—ROO• for TEA, and along path2, they are ROOH—O—ROO• for DME and R_2—P—ROO• for TMP. By comparing the results of ether-type key intermediates, the Bader charge of O40 in ROOH—S—ROO• (the target oxygen atom that hydrogen is shifted to) is 0.22 e^-, which is 0.03 e^- more than that in ROOH—O—ROO•. Larger Bader charge implies the target oxygen atom has a smaller capacity to accept a hydrogen atom; thus, ROOH—S—ROO• is less attractive to a hydrogen atom. Additionally, the H-shift distance is 2.74 Å in ROOH—S—ROO•, which is longer than that (2.59 Å) in ROOH—O—ROO•. This also adds difficulty for H-shift steps to occur. The above reasons attribute to why DMS and DME share similar ether structures but carry out different autoxidation paths. The same explanation is also appropriate for TEA and TMP. The above conclusion inspires us to further explore specific influences of the two autoxidation paths on cooling RFE of related VOC-Kao particles.

Our present results show that the heterogeneous autoxidation of the four VOCs is accelerated at different levels on the Kao surface, which is proven by a larger k of rate-limiting H-shift steps occurring on the Kao surface (Table S2). Specifically, the k of heterogeneous autoxidation is 4 orders higher for DME [43] than that of homogeneous autoxidation, and for DMS [43] and TEA, their k of heterogeneous autoxidation is separately 3 and 2 orders higher.

3.3 | Strengthened Light Scattering

Refractive index (n) and extinction coefficient (p) together determine light scattering of particles. Under visible wavelengths (500–700 nm), we first compare the changes in the two optical parameters with the increase in OS for each VOC-Kao particle (Figure S3). Results show, along any autoxidation pathway, the extinction coefficient (p) values for VOC-Kao exhibited slight fluctuations within the range of 0.001–0.002 as the oxidation state (OS) increased. The extinction coefficient (p) values exhibited only a transient increase, reaching levels between 0.001 and 0.010, which was attributed to the formation of R• radicals (blue lines in Figure S3). This indicates that neither VOC uptake nor autoxidation significantly affects the extinction of Kao particles. Additionally, given the small magnitude of p, its contribution to light scattering evaluations can be considered negligible. By contrast, during the progression along either autoxidation path, the n values of the resulting species were significantly higher than those of the initial Kao and VOC-Kao at every oxidation state (OS) (Figure S4). Our calculations suggest that the refractive index of Kao particles increases as a result of interactions with the four VOCs, encompassing both their uptake and associated autoxidation processes. Furthermore, throughout the oxidation states (OS) examined on both autoxidation pathways, the value of n consistently exceeded that of p by roughly three to four orders of magnitude. Accordingly, VOC-Kao predominantly exhibits strong refraction throughout the entire autoxidation process. This is consistent with the experimental observations of Flores et al. [44], He et al. [17], and He et al. [45].

We next put emphasis on n changes. Figure 6 compares the n changes with OS along path1 and path2. Firstly, for each VOC-Kao particle, the n exhibited a stepwise increase with increasing oxidation state (OS). Specifically, along path1, n for DMS grows by from 1.245 to 1.267 (Figure 6a) and for TEA rises from 1.262 to 1.286 (Figure 6b); and, along path2, DME increases from 1.231 to 1.241 (Figure 6c) and for TMP grows from 1.256 to 1.282 (Figure 6d). These results indicate that n is positively correlated with OS. Moreover, the largest Δn ranks in the order of TEA (path1) > DMS (path1) and TMP (path2) > DME (path2). Computational results suggest that, for a given autoxidation pathway, the heterogeneous autoxidation of alkane-type VOCs results in a greater enhancement of the n than that observed for ether-type VOCs.

To reveal the intrinsic correlation between n and VOC types, we analyze the relationship between molecular structure parameters of VOCs and OS by using quantitative structure–property relationship (QSPR) method [46]. The molecular structure parameters include unsaturation (μ), polarizability (α), and molar mass (M) of all oxidation products with different OS. Therein, $\alpha = 1.51(\#C) + 0.17(\#H) + 0.57(\#O) + 1.05(\#N) + 2.99(\#S) + 2.48(\#P) + 0.32$, and $\mu = (\#C + 1) - 0.5(\#H - \#N \text{ or } \#P)$, where #atom represents the number of specific atoms. The increments of these parameters are

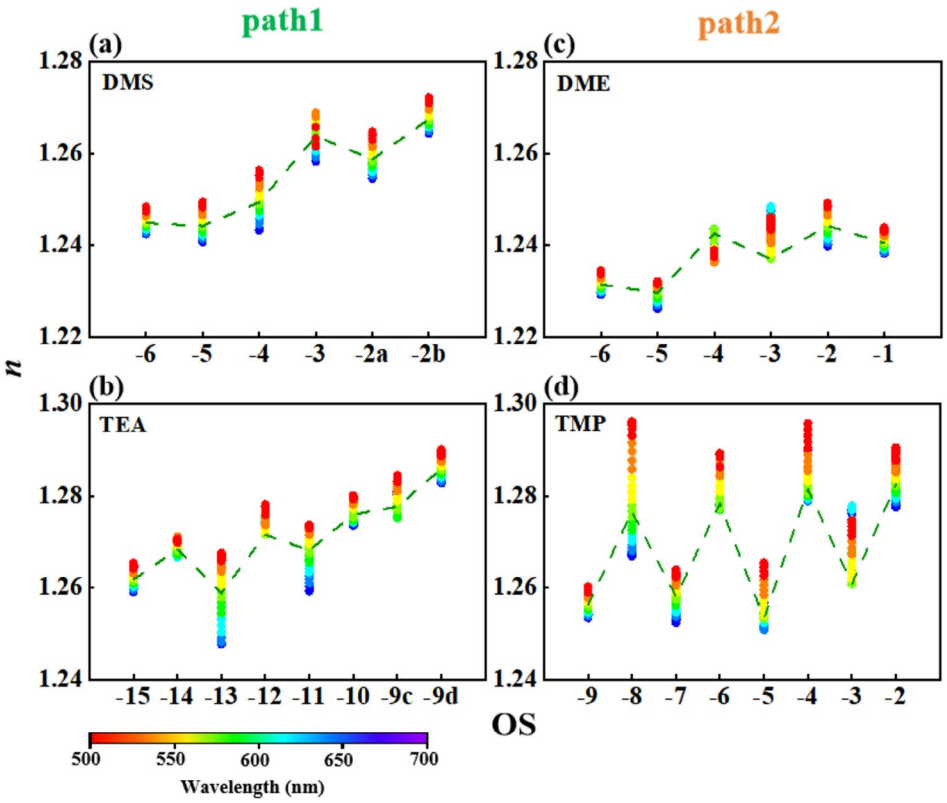

FIGURE 6 | The *n* changes of VOC-Kao particles with increased OS of (a) DMS (b) TEA (c) DME and (d) TMP at visible wavelengths of 500–700 nm. The green line indicates the trendline at 589 nm.

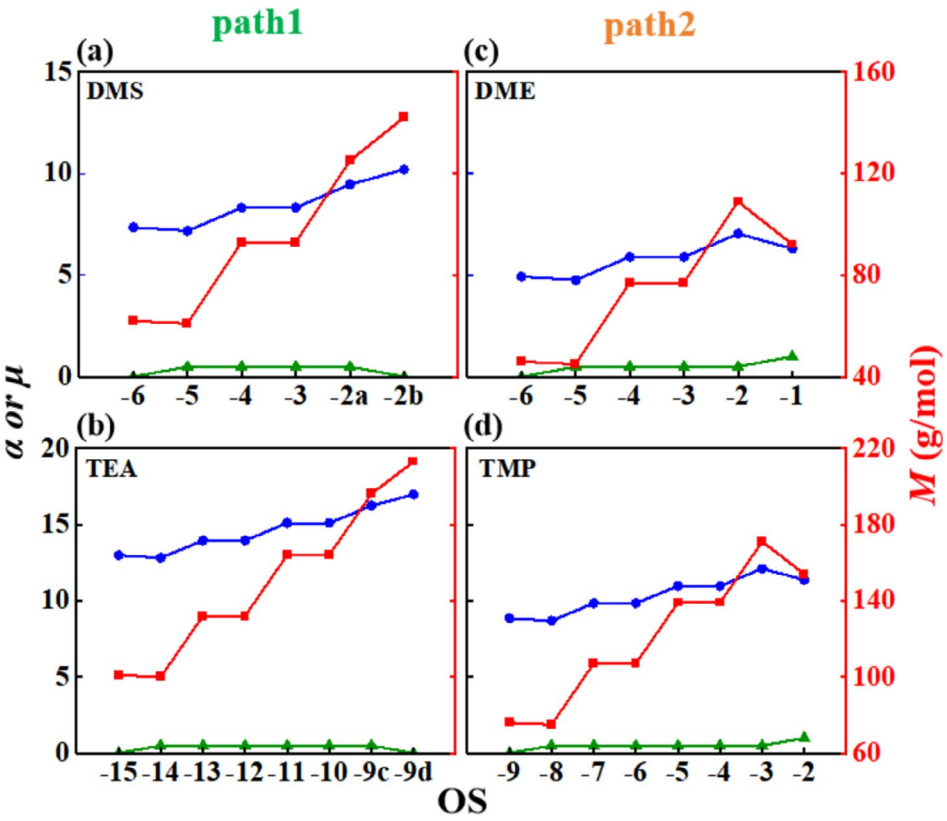

FIGURE 7 | The changes of molecular structure parameters with the increased OS of (a) DMS, (b) TEA, (c) DME and (d) TMP. The blue, green and red lines represent α, μ and M respectively.

written as $\Delta\mu$, $\Delta\alpha$ and ΔM, respectively. As displayed in Figure 7, for each VOC, μ almost keeps constant at 0.5 at variable OS values, indicating no contributions to Δn. Comparatively, α and M show significant increased trends with OS, and the trendline shapes are similar to that of n to the same VOC-Kao particles. This explains that α and M together determine Δn.

Next, the parameter M was analyzed along the two distinct autoxidation pathways. It was found that M for DMS and TEA displayed comparable trends of increase (path1, Figure 7a,b). This is because they share the same autoxidation path1. However, ΔM of TEA is larger than that of DMS, which is determined by two more oxygen contents in the former's HOMs product. As the increased trend of $\Delta\alpha$ is identical with ΔM to the same VOC, higher oxygen content also explains the larger $\Delta\alpha$ of TEA than that of DMS. This rule also applies to DME's and TMP's results (path2, Figure 7c,d). Accordingly, the n increment is dominantly caused by oxygen content accumulations, which results from O_2-addition steps. As concluded above, along the same heterogeneous autoxidation path, alkane-type VOCs proceed with more O_2-addition steps than ether-type VOCs. Therefore, this finally determines that the heterogeneous autoxidation of alkane-type VOCs increases n more significantly than ether-type VOCs.

4 | Conclusions

This study establishes a hierarchical relationship: The molecular structure of VOCs (alkane vs. ether) dictates the autoxidation pathways, characterized by differing extents of O_2-addition. This leads to the formation of HOMs with distinct oxidation states, molar masses, and polarizabilities. Consequently, these HOM properties drive variations in the light-scattering parameters (refractive index) of associated mineral particles. Specifically, computations indicate that alkane-type VOCs yield HOMs with higher oxygen content, facilitated by their structural propensity for H-shift and O_2-addition reactions. This results in a calculated enhancement of light scattering (refractive index) by 0.019–0.045 relative to HOMs derived from ether-type VOCs, under visible light conditions. These findings underscore the critical influence of the initial VOC structure on the optical properties of aerosols and their climate-relevant radiative forcing, thereby providing a mechanistic framework for predicting changes in relative forward scattering efficiency (RFE) in polluted, mineral-dominated atmospheres.

By combining QSPR modeling with heterogeneous autoxidation mechanisms, this study established quantitative relationships between the autoxidation process and refractive index. It was determined that the refractive index primarily correlates with the polarizability (α), degree of unsaturation (μ), and relative molecular mass (M) of VOCs. As the oxidation degree of VOCs on mineral particle surfaces increases, significant increases in $\Delta\alpha$ and ΔM of VOCs are observed. This leads to an increased refractive index of the VOC-mineral particle mixture compared to the original pristine mineral particles, suggesting that such heterogeneous autoxidation processes enhance their light-scattering ability. These findings not only enrich the understanding of heterogeneous oxidation mechanisms of VOCs but can also be extended to predict the impact of other structurally similar VOCs on the refractive index of mineral particles. Furthermore, the quantitative structure-relationship provided by this study offers key parameters for climate models to accurately assess their radiative effects.

Acknowledgments

This work is supported by NSFC (42277081 and 42077189), the Basic and Applied Basic Research Fund Project of Guangdong Province (2024A1515012691), the National Key Research and Development Program of China (2022YFC3105600), and the GuangZhou Basic and Applied Basic Research Foundation (2025A04J5188).

Conflicts of Interest

The authors declare no conflicts of interest.

Data Availability Statement

The data that support the findings of this study are available from the corresponding author upon reasonable request.

References

1. W. Nie, A. J. Ding, T. Wang, et al., "Polluted Dust Promotes New Particle Formation and Growth," *Scientific Reports* 4 (2014): 6634.

2. Y. P. Ji, X. Y. Chen, Y. Q. Xiao, et al., "Assessing the Role of Mineral Particles in the Atmospheric Photooxidation of Typical Carbonyl Compound," *Journal of Environmental Sciences* 105 (2021): 56–63.

3. Z. M. Chen, C. Y. Jie, S. Li, et al., "Heterogeneous Reactions of Methacrolein and Methyl Vinyl Ketone: Kinetics and Mechanisms of Uptake and Ozonolysis on Silicon Dioxide," *Journal of Geophysical Research: Atmospheres* 113, no. D22 (2008): 2007JD009754.

4. M. J. Yao, Y. M. Ji, H. H. Wang, Z. M. Ao, G. Y. Li, and T. C. An, "Adsorption Mechanisms of Typical Carbonyl-Containing Volatile Organic Compounds on Anatase TiO2 (001) Surface: A DFT Investigation," *Journal of Physical Chemistry C* 121, no. 25 (2017): 13717–13722.

5. P. F. Tian, L. Zhang, X. J. Cao, et al., "Enhanced Bottom-Of-The-Atmosphere Cooling and Atmosphere Heating Efficiency by Mixed-Type Aerosols: A Classification Based on Aerosol Nonsphericity," *Journal of the Atmospheric Sciences* 75, no. 1 (2018): 113–124.

6. P. Tian, L. Zhang, J. Ma, et al., "Radiative Absorption Enhancement of Dust Mixed With Anthropogenic Pollution Over East Asia," *Atmospheric Chemistry and Physics* 18, no. 11 (2018): 7815–7825.

7. W. Zhang, J. Mai, Z. Fan, et al., "EGUsphere 2024," (2024), 1–17.

8. F. Bianchi, T. Kurtén, M. Riva, et al., "Highly Oxygenated Organic Molecules (HOM) From Gas-Phase Autoxidation Involving Peroxy Radicals: A Key Contributor to Atmospheric Aerosol," *Chemical Reviews* 119, no. 6 (2019): 3472–3509.

9. J. D. Crounse, L. B. Nielsen, S. Jorgensen, H. G. Kjaergaard, and P. O. Wennberg, "Autoxidation of Organic Compounds in the Atmosphere," *Journal of Physical Chemistry Letters* 4, no. 20 (2013): 3513–3520.

10. M. Ehn, J. A. Thornton, E. Kleist, et al., "A Large Source of Low-Volatility Secondary Organic Aerosol," *Nature* 506, no. 7489 (2014): 476–479.

11. S. M. Wang, Q. Z. Zhang, G. Q. Wang, Y. Y. Wei, W. X. Wang, and Q. Wang, "The Neglected Autoxidation Pathways for the Formation of Highly Oxygenated Organic Molecules (HOMs) and the Nucleation of the HOMs Generated by Limonene," *Atmospheric Environment* 304 (2023): 119727.

12. Y. M. Ji, X. Y. Chen, Y. X. Li, et al., "The Mixing State of Mineral Dusts With Typical Anthropogenic Pollutants: A Mechanism Study," *Atmospheric Environment* 209 (2019): 192–200.

13. M. A. Obregón, S. Pereira, V. Salgueiro, et al., "Aerosol Radiative Effects During Two Desert Dust Events in August 2012 Over the Southwestern Iberian Peninsula," *Atmospheric Research* 153 (2015): 404–415.

14. Z. Wang, X. L. Pan, I. Uno, et al., "Importance of Mineral Dust and Anthropogenic Pollutants Mixing During a Long-Lasting High PM Event Over East Asia," *Environmental Pollution* 234 (2018): 368–378.

15. L. Poulain, A. Tilgner, M. Brüggemann, et al., "Particle-Phase Uptake and Chemistry of Highly Oxygenated Organic Molecules (HOMs) From α-Pinene OH Oxidation," *Journal of Geophysical Research: Atmospheres* 127 (2022): 16.

16. J. Tröstl, W. K. Chuang, H. Gordon, et al., "The Role of Low-Volatility Organic Compounds in Initial Particle Growth in the Atmosphere," *Nature* 533, no. 7604 (2016): 527.

17. Q. He, N. Bluvshtein, L. Segev, et al., "Evolution of the Complex Refractive Index of Secondary Organic Aerosols During Atmospheric Aging," *Environmental Science & Technology* 52, no. 6 (2018): 3456–3465.

18. A. T. Lambe, C. D. Cappa, P. Massoli, et al., "Relationship Between Oxidation Level and Optical Properties of Secondary Organic Aerosol," *Environmental Science & Technology* 47, no. 12 (2013): 6349–6357.

19. X. W. Chen, L. Du, Z. M. Yang, et al., "Interaction Between Marine and Terrestrial Biogenic Volatile Organic Compounds: Non-linear Effect on Secondary Organic Aerosol Formation," *Atmospheric Environment* 338 (2024): 120868.

20. W. H. Brune, T. B. Nguyen, P. O. Wennberg, J. D. Crounse, and D. O. Miller, "Comparison of Isoprene Chemical Mechanisms With Chamber and Field Observations," *ACS Earth and Space Chemistry* 8, no. 11 (2024): 2256–2269.

21. K. H. Moller, T. Berndt, and H. G. Kjaergaard, "Correction to "Atmospheric Autoxidation of Amines"," *Environmental Science & Technology* 55, no. 6 (2021): 4079.

22. E. R. Kjærgaard, K. H. Møller, T. Berndt, and H. G. Kjaergaard, "Highly Efficient Autoxidation of Triethylamine," *Journal of Physical Chemistry A* 127 (2023): 8623–8632.

23. X. L. Ge, A. S. Wexler, and S. L. Clegg, "Atmospheric Amines—Part I. A Review," *Atmospheric Environment* 45, no. 3 (2011): 524–546.

24. T. Berndt, W. Scholz, B. Mender, et al., "Fast Peroxy Radical Isomerization and OH Recycling in the Reaction of OH Radicals With Dimethyl Sulfide," *Journal of Physical Chemistry Letters* 10, no. 21 (2019): 6478–6483.

25. Q. Ye, M. B. Goss, G. Isaacman-VanWertz, et al., "Organic Sulfur Products and Peroxy Radical Isomerization in the OH Oxidation of Dimethyl Sulfide," *ACS Earth and Space Chemistry* 5, no. 8 (2021): 2013–2020.

26. S. N. Wang and L. M. Wang, "The Atmospheric Oxidation of Dimethyl, Diethyl, and Diisopropyl Ethers. The Role of the Intramolecular Hydrogen Shift in Peroxy Radicals," *Physical Chemistry Chemical Physics* 18, no. 11 (2016): 7707–7714.

27. M. Tang, D. J. Cziczo, and V. H. Grassian, "Interactions of Water With Mineral Dust Aerosol: Water Adsorption, Hygroscopicity, Cloud Condensation, and Ice Nucleation," *Chemical Reviews* 116, no. 7 (2016): 4205–4259.

28. G. Kresse and J. Furthmüller, "Efficiency of Ab-Initio Total Energy Calculations for Metals and Semiconductors Using a Plane-Wave Basis Set," *Computational Materials Science* 6, no. 1 (1996): 15–50.

29. J. P. Perdew, J. A. Chevary, S. H. Vosko, et al., "Atoms, Molecules, Solids, and Surfaces: Applications of the Generalized Gradient Approximation for Exchange and Correlation," *Physical Review B: Condensed Matter* 46, no. 11 (1992): 6671–6687.

30. S. Grimme, J. Antony, S. Ehrlich, and H. Krieg, "A Consistent and Accurateab Initioparametrization of Density Functional Dispersion Correction (DFT-D) for the 94 Elements H-Pu," *Journal of Chemical Physics* 132, no. 15 (2010): 154104.

31. D. Tunega, M. H. Gerzabek, and L. Böhm, "Theoretical Study on Adsorption of Halogenated Benzenes on Montmorillonites Modified With M(I)/M(II) Cations," *Journal of Computational Chemistry* 46, no. 3 (2025): e70042.

32. G. Henkelman, B. P. Uberuaga, and H. Jónsson, "A Climbing Image Nudged Elastic Band Method for Finding Saddle Points and Minimum Energy Paths," *Journal of Chemical Physics* 113, no. 22 (2000): 9901–9904.

33. A. Fernández-Ramos, B. A. Ellingson, R. Meana-Pañeda, J. M. C. Marques, and D. G. Truhlar, "Symmetry Numbers and Chemical Reaction Rates," *Theoretical Chemistry Accounts* 118 (2007): 813–826.

34. J. H. Kroll, C. Y. Lim, S. H. Kessler, and K. R. Wilson, "Heterogeneous Oxidation of Atmospheric Organic Aerosol: Kinetics of Changes to the Amount and Oxidation State of Particle-Phase Organic Carbon," *Journal of Physical Chemistry A* 119, no. 44 (2015): 10767–10783.

35. M. Fox and G. F. Bertsch, "Optical Properties of Solids," *American Journal of Physics* 70, no. 12 (2002): 1269–1270.

36. M. Gajdoš, K. Hummer, G. Kresse, J. Furthmüller, and F. Bechstedt, "Linear Optical Properties in the Projector-Augmented Wave Methodology," *Physical Review B: Condensed Matter* 73, no. 4 (2006): 45112–45121.

37. V. Wang, N. Xu, J.-C. Liu, G. Tang, and W.-T. Geng, "VASPKIT: A User-Friendly Interface Facilitating High-Throughput Computing and Analysis Using VASP Code," *Computer Physics Communications* 267 (2021): 267–286.

38. A. M. El-Nahas, T. Uchimaru, M. Sugie, K. Tokuhashi, and A. Sekiya, "Hydrogen Abstraction From Dimethyl Ether (DME) and Dimethyl Sulfide (DMS) by OH Radical: A Computational Study," *Journal of Molecular Structure: THEOCHEM* 722, no. 1–3 (2005): 9–19.

39. C. Han, J. J. Geng, Y. N. Hong, et al., "Free Atmospheric Phosphine Concentrations and Fluxes in Different Wetland Ecosystems, China," *Environmental Pollution* 159, no. 2 (2011): 630–635.

40. R. A. Scanza, N. Mahowald, S. Ghan, et al., "Modeling Dust as Component Minerals in the Community Atmosphere Model: Development of Framework and Impact on Radiative Forcing," *Atmospheric Chemistry and Physics* 15, no. 1 (2015): 537–561.

41. Z. F. Tan, F. Rohrer, K. D. Lu, et al., "Wintertime Photochemistry in Beijing: Observations of ROx Radical Concentrations in the North China Plain During the BEST-ONE Campaign," *Atmospheric Chemistry and Physics* 18, no. 16 (2018): 12391–12411.

42. T. Berndt, J. Chen, E. R. Kjærgaard, et al., "Hydrotrioxide (ROOOH) Formation in the Atmosphere," *Science* 376, no. 6596 (2022): 979–982.

43. K. H. Moller, T. Berndt, and H. G. Kjaergaard, "Atmospheric Autoxidation of Amines," *Environmental Science & Technology* 54, no. 18 (2020): 11087–11099.

44. J. M. Flores, D. F. Zhao, L. Segev, et al., "Evolution of the Complex Refractive Index in the UV Spectral Region in Ageing Secondary Organic Aerosol," *Atmospheric Chemistry and Physics* 14, no. 11 (2014): 5793–5806.

45. Q. F. He, C. L. Li, K. Siemens, et al., "Optical Properties of Secondary Organic Aerosol Produced by Photooxidation of Naphthalene Under NOx Condition," *Environmental Science & Technology* 56, no. 8 (2022): 4816–4827.

46. H. Redmond and J. E. Thompson, "Evaluation of a Quantitative Structure–Property Relationship (QSPR) for Predicting Mid-Visible Refractive Index of Secondary Organic Aerosol (SOA)," *Physical Chemistry Chemical Physics* 13, no. 15 (2011): 6872–6882.

Supporting Information

Additional supporting information can be found online in the Supporting Information section. **Data S1.**